Estimating confidence intervals around relative humidity profiles from satellite observations: Application to the SAPHIR sounder

Hélène Brogniez, Renaud Fallourd, Cécile Mallet, Ramses Sivira, Christophe Dufour

Estimating Confidence Intervals around Relative Humidity Profiles from Satellite Observations: Application to the SAPHIR Sounder

HÉLÈNE BROGNIEZ, RENAUD FALLOURD, CÉCILE MALLET, RAMSÈS SIVIRA,[a] AND CHRISTOPHE DUFOUR

LATMOS/IPSL, UVSQ Université Paris-Saclay, UPMC Université Paris 06, CNRS, Guyancourt, France

(Manuscript received 20 November 2015, in final form 7 March 2016)

ABSTRACT

A novel scheme for the estimation of layer-averaged relative humidity (RH) profiles from spaceborne observations in the 183.31-GHz line is presented. Named atmospheric relative humidity profiles including analysis of confidence intervals (ARPIA), it provides for each vector of observations the parameters of the distribution of the RH instead of its expectation, as is usually done by the current methods. The profiles are composed of six layers distributed between 100 and 950 hPa. The approach combines the six channels of the Sondeur Atmosphérique du Profil d'Humidité Intertropical par Radiométrie (SAPHIR) instrument on board the *Megha-Tropiques* satellite and the generalized additive model for location, scale and shape (GAMLSS) method to infer the parametric distributions, assuming that they follow a Gaussian law. The knowledge of the conditional uncertainty is an asset in the evaluation using radiosounding profiles of RH with a dedicated Bayesian method. Taking the uncertainties into account in both the ARPIA estimates and the in situ measurements yields biases, root-mean-square, and correlation coefficients in the range of −0.56% to 9.79%, 1.58% to 13.32%, and 0.55 to 0.98, respectively, with the largest biases being obtained over the continent, in the midtropospheric layers.

1. Introduction

The distribution and variability of water vapor is a key parameter of the climate system, through radiation processes (Spencer and Braswell 1997; Allan et al. 1999; Held and Soden 2000; Pierrehumbert 2011; Allan 2012), thermodynamics and phase changes (Pierrehumbert and Roca 1998; John and Soden 2006; Held and Soden 2006; Stevens and Bony 2013), and dynamical flows (Galewsky et al. 2005; Roca et al. 2005; Brogniez et al. 2009; Sherwood et al. 2010). Even if the underlying physics of some of these processes are well understood, such as the Clausius–Clapeyron equation, which constrains the moisture content of the atmosphere (Stevens and Bony 2013), filling the gaps requires a continuous monitoring of the atmospheric water vapor.

Spaceborne observations complete the network of radiosounding stations since the 1970s and provide numerous constraints for numerical weather prediction (NWP) models through data assimilation (e.g., Andersson et al. 2005). Among the current spaceborne observations performed over a wide range of frequencies, it has been shown that microwave sounders provide the main source of constraints on the vertical profiles of atmospheric relative humidity (RH) within NWP models (Andersson et al. 2007; Radnóti et al. 2010). In fact, observations in the 183.31-GHz rotational transition line of the water molecule allow for the study of RH even in the presence of low-level clouds (Isaacs and Deblonde 1987). High-level clouds combine increased absorption by water vapor within the saturated clouds and scattering by precipitating particles (icy or water droplets; Burns et al. 1997; Houshangpour et al. 2005; Hong et al. 2005; Buehler et al. 2008). Such features of the microwave radiation allows for the study of mechanisms at play around the convective cores (Bretherton et al. 2004; Hong et al. 2008; Zelinka and Hartmann 2009; Chae et al. 2011).

Beside the assimilation of the raw observations for NWP purposes, measurements in the 183.31-GHz line are used to estimate the relative humidity profiles, and various inversion techniques exist. Multivariate regression techniques (Rosenkranz et al. 1982; Sivira et al.

[a] Current affiliation: Meteo Protect SAS, Paris, France.

Corresponding author address: Hélène Brogniez, LATMOS, IPSL, 11 Boulevard d'Alembert, 78280 Guyancourt, France.
E-mail: helene.brogniez@latmos.ipsl.fr

DOI: 10.1175/JTECH-D-15-0237.1

2015), and in particular neural networking (Cabrera-Mercader and Staelin 1995; Karbou et al. 2005; Aires et al. 2013), embed all the atmospheric characteristics in a statistical training base. The *N*-dimensional variational schemes include the physical constraints in the first guesses and in the iterative procedures (Wilheit 1990; Blankenship et al. 2000; Liu and Weng 2005), while multispectral methods combining infrared and microwave measurements have been mainly developed to optimize the retrievals of the cloud-free scenes (Blackwell and Chen 2006). Hence, the recent National Oceanic and Atmospheric Administration (NOAA) Unique Cross-Track Infrared Sounder (CrIS)/Advanced Technology Microwave Sounder (ATMS) processing system (NUCAPS) generates profiles of moisture on board the *Suomi–National Polar Orbiting Partnership* (*Suomi-NPP*) satellite with a global root-mean-square (RMS) difference around 30% in the midtroposphere and around 20% toward the surface (Nalli et al. 2013).

Overall, the methods of retrieval of a geophysical variable $\mathscr{X}$ from satellite observations provide a conditional estimate of the expectation of $\mathscr{X}$ given a set of inputs (restricted or not to the satellite data): here we propose an estimation of the parameters of the distribution of $\mathscr{X}$ that can be interpreted as a confidence interval of the retrieved value. The data used to design and test the retrieval scheme are presented in section 2. The approach used to estimate the conditional mean and standard deviation is introduced in section 3, together with the computation of the uncertainty of the observations. Section 4 is dedicated to the results obtained using *Megha-Tropiques* observations: a comparison of a set of radiosonde measurements and a snapshot of a tropical cyclone. Finally, some conclusions are drawn and a few perspectives are discussed in section 5.

2. Data

a. SAPHIR observations

Sondeur Atmosphérique du Profil d'Humidité Intertropical par Radiométrie (SAPHIR) is a passive microwave sounder that measures the upwelling radiation in the 183.3-GHz water vapor absorption line. As part of the *Megha-Tropiques* payload, SAPHIR has six double-sideband channels located close to the line center (channel 1 at 183.31 ± 0.2 GHz) down to the wings (channel 6 at 183.31 ± 11 GHz). It is a cross-track radiometer that observes the earth's atmosphere with a scan angle of ±42.96°, a footprint size at nadir of 10 × 10 km^2, and a 1700-km swath made of scan lines containing 130 nonoverlapping footprints. Details of the instrument and its channel characteristics are described in many publications (Karouche et al. 2012; Brogniez et al. 2013; Roca et al. 2015; see also http://smsc.cnes.fr/MEGHAT/index.htm for monthly technical updates of the instrument).

Ice layers in the upper parts of clouds and convective rainfall have a clear signature in 183-GHz channels (Hakkarinen and Adler 1988; Burns et al. 1997), and the detection schemes of such scenes have been developed for the Advanced Microwave Sounding Unit-B (AMSU-B; Greenwald and Christopher 2002; Hong et al. 2005) and adapted for the slightly different channels of SAPHIR (Sivira et al. 2015). In fact, because SAPHIR measurements are almost insensitive to the presence of nonscattering clouds (either from ice or from rainfall), the RH retrieval method is applied to all pixels, in an undifferentiated manner, as soon as the detection scheme mentioned above considers a pixel as nonconvective.

In addition, information from the cloud cover within every pixel of SAPHIR is provided by data from the various geostationary satellites observing the tropical belt [GOES-West and GOES-East of NOAA, the Meteorological Satellite (Meteosat) of the European Organisation for the Exploitation of Meteorological Satellites (EUMETSAT), and the Multifunctional Transport Satellite (MTSAT) of the Japan Meteorological Agency (JMA)]. The algorithm developed by the Satellite Application Facility on Support to Nowcasting and Very Short Range Forecasting (SAF NWC) has been adapted to each satellite, thus giving a consistent cloud analysis. The method and a comparison to the Cloud–Aerosol Lidar with Orthogonal Polarization (CALIOP) of the *CALIPSO* satellite are described in Sèze et al. (2015). Therefore, the individual cloud analysis from each geostationnary pixel (up to 40 pixels) is kept within every pixel of SAPHIR and is used to classify the retrieval in terms of cloudy/cloud-free types.

b. Radiosounding profiles

Here we use two distinct sets of radiosonde profiles: a synthetic training set used to overcome the issue of the number of space/time collocations between *Megha-Tropiques* observations and radiosonde (RS) profiles representative of the tropical atmosphere, and a set of field campaign measurements for the application to real data.

1) The synthetic training set

This study follows the work described in Sivira et al. (2015) dedicated to the design of a layer-averaged RH profile algorithm. Therefore, the synthetic dataset is the same and has the same purpose of statistical training and validation. Hence, in order to overcome the size issue of a training dataset made of *Megha-Tropiques*

observations collocated in space and time with high-quality RS profiles, we associated the thermodynamic profiles extracted from the Analyzed Radiosoundings Archive (ARSA; http://ara.abct.lmd.polytechnique.fr/index.php?page=arsa) with a radiative transfer model used to provide the corresponding SAPHIR brightness temperatures (BTs). The various quality steps applied to the RS profiles of ARSA can be found in Sivira et al. (2015).

As in Sivira et al. (2015), the simulation of SAPHIR BTs from the RS profile is performed using version 9.3 of the Radiative Transfer for the Television and Infrared Observation Satellite (TIROS) Operational Vertical Sounder (RTTOV) fast radiative transfer model (Matricardi et al. 2004). The surface emissivity is either prescribed using the 10-yr emissivity atlas of Prigent et al. (2006) for the continental cases or computed within RTTOV with the Fast Emissivity Model-3 (FASTEM-3; Deblonde and English 2000) and 10-m wind speed. The 1990–2007 archive of ARSA is considered and only profiles restricted to the 30°N/30°S belt are kept. As discussed in Sivira et al. (2015), this subset of ARSA has the known characteristics of the tropical atmosphere. However, only a few cases sample the extremely dry (total column water vapor < 20 mm) and very moist (total column water vapor > 80 mm) columns.

2) Field campaigns measurements

RS profiles obtained from two field campaigns are explored and considered as reference profiles for the evaluation of the method. The two sets are based on measurements by Vaisala RS92-SGPD (RS92) probes that offer consistency in data quality.

- Cooperative Indian Ocean Experiment on Intraseasonal Variability in the Year 2011 (CINDY2011)/Dynamics of the Madden–Julian Oscillation (DYNAMO)/ARM Madden–Julian oscillation (MJO) Investigation Experiment (AMIE; winter 2011/12): Between September 2011 and March 2012, the field campaign CINDY2011–DYNAMO–AMIE (CDA) took place over the Indian Ocean with the aim of a better description of the MJO and its key processes. CINDY2011 (see http://www.jamstec.go.jp/iorgc/cindy/), DYNAMO (see http://www.eol.ucar.edu/projects/dynamo/), and AMIE (see http://campaign.arm.gov/amie/) gathered a radar network (island and shipborne), a ship/mooring network, in situ measurements from aircrafts (microphysics probes and radar), and 51 priority sounding sites (Ciesielski et al. 2014). Here, we use the RS92 selected by Clain et al. (2015) that is extracted from level 3 of the CDA upper-air database, reasonably collocated in space (within a 50-km radius area) and time (within a ±45-min window), with SAPHIR observations. Ouagadougou (summer 2012): A *Megha-Tropiques* validation campaign took place thanks to a supersite located in Ouagadougou, Burkina Faso (12.37°N, 1.54°W), between April and August 2012. It gathered a polarimetric radar (X-band radar Xport), a densified rain gauge network, and two intense phases of radiosoundings. This campaign is the result of a strong collaboration between the French Institut de Recherche pour le Développement (IRD), the National Weather Service [Direction Générale de la Météorologie (DGM)] of Burkina Faso, and the Agency for Aerial Navigation Safety in Africa and Madagascar [Agence pour la Sécurité de la Navigation Aérienne en Afrique et à Madagascar (ASECNA). During this campaign, 55 RS92 probes were launched at *Megha-Tropiques* overpasses and during a premonsoon period (29 May–11 June 2012) and a monsoonal period (17 July–1 August 2012).

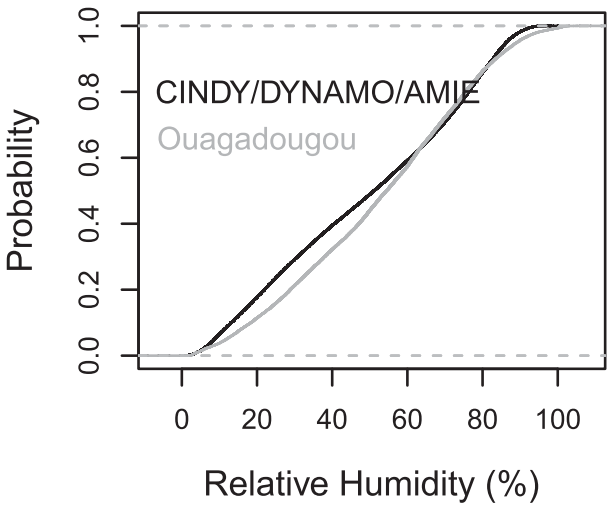

FIG. 1. Cumulative distribution functions of RH (%RH) within the CDA set (black curve) and within the Ouagadougou set (gray curve).

These two sets have been already explored for the evaluation of the upper-tropospheric humidity products derived from SAPHIR (Brogniez et al. 2015), and here we use the entire profiles. The cumulative distribution functions of the RH of these two sets are presented in Fig. 1 and show that, overall, the CDA RS probes sample more cases with RH between 10% and 40% than in Ouagadougou.

3) General characteristics

We decompose the troposphere into six layers, following the method described by Sivira et al. (2015): the upper and lower bounds of the layers are defined

TABLE 1. Statistics of the different GAM-based estimations of the six-layer RH profile (radiosoundings from the 1990–2007 period) for the oceanic training and for the continental training. The mean (% RH) and the variance (% RH) of the residuals (estimated minus observed RH), and the Pearson correlation coefficient are given.

	Validation of the models					
	Mean of residuals (%)		Std dev of residuals (%)		Correlation (Pearson)	
Layer	Oceanic	Continental	Oceanic	Continental	Oceanic	Continental
100–200 hPa (L1)	1.58	1.51	7.1	7.2	0.84	0.84
250–350 hPa (L2)	0.80	0.09	3.9	3.6	0.94	0.95
400–600 hPa (L3)	1.80	−0.26	4.6	5.2	0.97	0.93
650–700 hPa (L4)	2.00	2.62	12.3	11.3	0.82	0.85
750–800 hPa (L5)	1.11	2.79	15.8	12.5	0.70	0.82
850–950 hPa (L6)	−1.50	3.70	12.5	14.8	0.72	0.74

from the patterns contained in the ARSA database, with a distinction between oceanic and continental situations. The original relative humidity profiles are vertically clustered thanks to self-organized maps (also known as Kohonen maps; Kohonen 1982) combined with a semiempirical iterative method in order to obtain layers with minimal variance of RH, as well as minimal mean–median distance. The six layers are defined in Table 1. The BTs are normalized (zero mean and unity variance). The retrieval technique is trained over a sampling of two-thirds of the ARSA database that has been randomly perturbed using the in-flight radiometric noises of SAPHIR channels (10 noisy reproductions of each state; see Sivira et al. 2015), and then tested over the remaining one-third of the database.

3. Uncertainty analysis

a. Rationale

A known feature of sounders is the evolution of the sensitivity functions (the RH Jacobians $\mathscr{J}_{RH} = \partial BT/\partial RH$) with the characteristics of the atmosphere under consideration (Schaerer and Wilheit 1979). This is illustrated by two tropical profiles in Fig. 2: when the atmosphere gets drier, the $\mathscr{J}_{RH}$ of SAPHIR widen and the peaks of the maxima shift downward. This is further generalized over the ARSA synthetic set in Fig. 3, which shows the distribution of the maxima of the $\mathscr{J}_{RH}$ according to the corresponding values of BT (computed at nadir). For instance, for C6 (183.31 ± 11 GHz) the warmest BTs (i.e., the driest profiles) are associated with low peaking $\mathscr{J}_{RH}$. Despite this feature, common to all microwave humidity

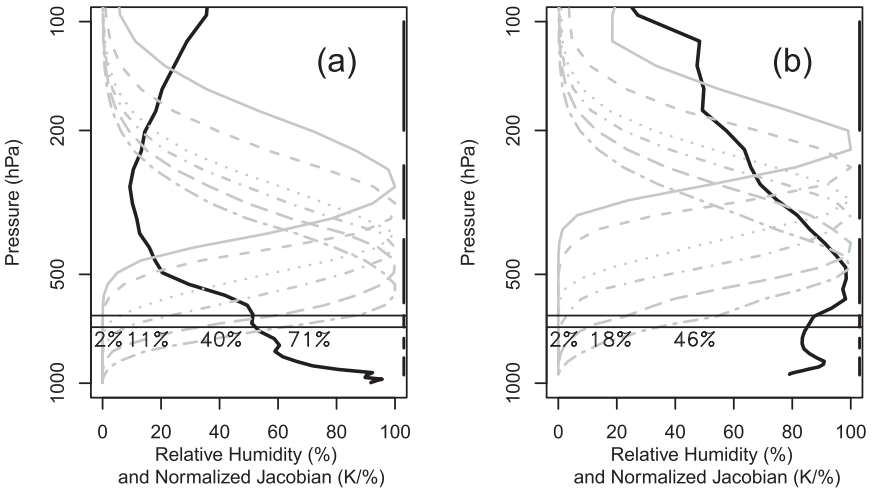

FIG. 2. Vertical profiles (log scale) of the six $\mathscr{J}_{RH}$ of SAPHIR for (a) dry and (b) moist atmospheres. The corresponding RH profile is the black line, and the gray curves are the $\mathscr{J}_{RH}$ for the six channels (C1: plain line, C2: dashed line, C3: dotted line, C4: dotted–dashed line, C5: long dashed line, C6: two dashed line). The vertical bars on the right-hand side indicate the six atmospheric layers. The mean relative contributions (%, if greater than 1%) of each $\mathscr{J}_{RH}$ in the global information of the 650–700-hPa layer are indicated as an illustration.

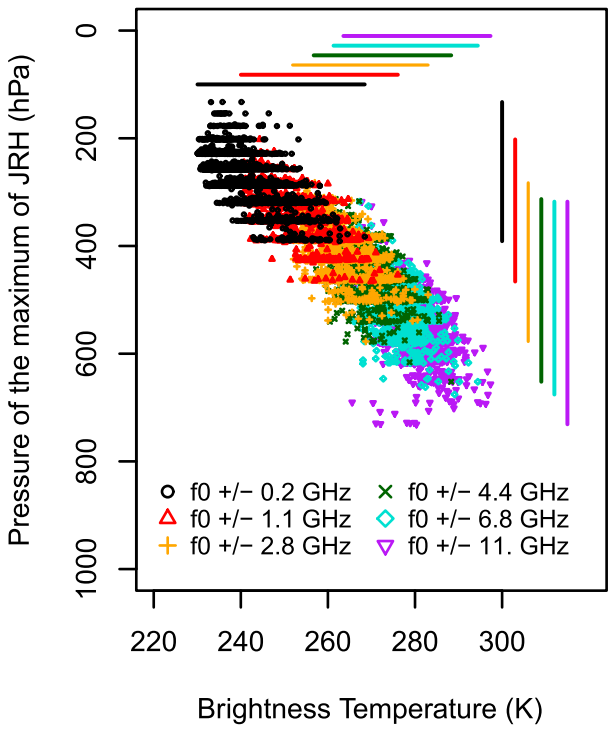

FIG. 3. Pressures of the maxima of the six $\mathscr{J}_{\mathrm{RH}}$ of SAPHIR over the ARSA subset according to the simulated BTs of the profiles. Term f_0 is the central frequency of SAPHIR, i.e., 183.31 GHz. The vertical and horizontal bars located on the right and on the top represent the ranges of values (minima and maxima) for the pressures and the BTs, respectively.

sensors, a few papers have already demonstrated the usefulness of SAPHIR measurements to estimate layer-averaged RH profiles (Aires et al. 2013; Brogniez et al. 2013; Gohil et al. 2013; Sivira et al. 2015), with an increased improvement of the retrievals with respect to the three-channel operational sensors toward the edges of the troposphere.

We follow the work of Brogniez et al. (2013) and Sivira et al. (2015), who opted for generalized additive models (GAMs; Hastie and Tibshirani 1987; Wood 2006) to retrieve RH layer-averaged profiles. A GAM is a nonparametric model that has the flexibility to depict any nonlinearity that is contained in the data used to calibrate, or train, the transfer function between a set of explanatory variables X_i and the explained variable Y. In such a model, the structure of each explanatory variable is assumed to be additive, which gives the form

$$g(\mathbb{E}(Y \mid \mathbf{X})) = \sum_{i=1}^{p} f_i(X_i) + \varepsilon, \qquad (1)$$

where $g(\cdot)$ is a link function between the expectation of Y conditionally on a p-dimensional explanatory variable $\mathbf{X}$ $(X_1, \ldots, X_p)$—say, $\mathbb{E}(Y \mid \mathbf{X})$—and a sum of $f_i(X_i)$ $(i = 1, \ldots, p)$. The functions $f_i(\cdot)$ are nonparametric functions with specific terms and coefficients that need to be defined. Finally, ε is a zero-mean Gaussian noise. Transposed to the present work, the p-dimensional explanatory variable $\mathbf{X}$ is the vector of **BT** (with $p = 6$) of SAPHIR for a given sample and the explained variable Y is the RH of an atmospheric layer k, noted RH^k $(k = 1, \ldots, 6)$. For each k, penalized regression cubic splines are used as the smoothing functions f_i^k and are estimated independently of the other covariates using a "back-fitting algorithm" (Hastie and Tibshirani 1990). The determination of the appropriate degree of smoothness of each spline is performed during the model-fitting step, through the minimization of the generalized cross-validation score (Wood 2004, 2006). Such a score is computed from the rotation of the data into a plane in which all the data have the same influence, followed by a leave-one-out procedure for the validation step of the estimated smoothing parameter. Figure 4 represents the f_i^k for each of the six atmospheric layers, using the statistical training dataset ARSA. The x axes correspond to each explanatory variable BT_i and the y axes give their relative contribution [i.e., the $f_i^k(\mathrm{BT}_i)$] to explain the RH^k. The gray envelop shows 2 times the standard error of the fitting procedure (the Cole and Green 1992) algorithm, based on derivatives of the likelihood function, or the Rigby and Stasinopoulos (1996) algorithm, based on semi-parametric additive models for the mean and variance), which can be increased by a lack of data in a given range (see the distribution of the gray ticks on the x axis) or by a distribution of data that does not allow convergence. Overall, but for two X_i for RH^1 ($X_2 = \pm 1.1$ GHz and $X_3 \pm 2.8$ GHz), the standard error is small. As expected by the sensitivity functions of SAPHIR (see Fig. 2), the dynamics of variation of every spline and its nonlinearities are strongly dependent to the atmospheric layer under consideration. For instance, the variability of RH^4 is driven by X_3 (± 2.8 GHz), X_4 (± 4.2 GHz), and X_5 (± 6.8 GHz), while RH^6 is mainly driven by X_6 (± 11 GHz).

Nevertheless, despite the strength of most retrieval techniques to capture the nonlinearities of the BT-to-RH inverse problem, such as GAMs, the dependence of the sensitivity functions of the instrument upon the atmospheric thermodynamics yields scene-dependent retrieval uncertainties. This is partly illustrated in Fig. 2 with the relative contribution of each $\mathscr{J}_{\mathrm{RH}}$ to the total signal (although it is not a simple addition, as discussed above), for an atmospheric layer covering 650–700 hPa. For this layer, the information content of the six channels is very different, thus yielding estimated RH with

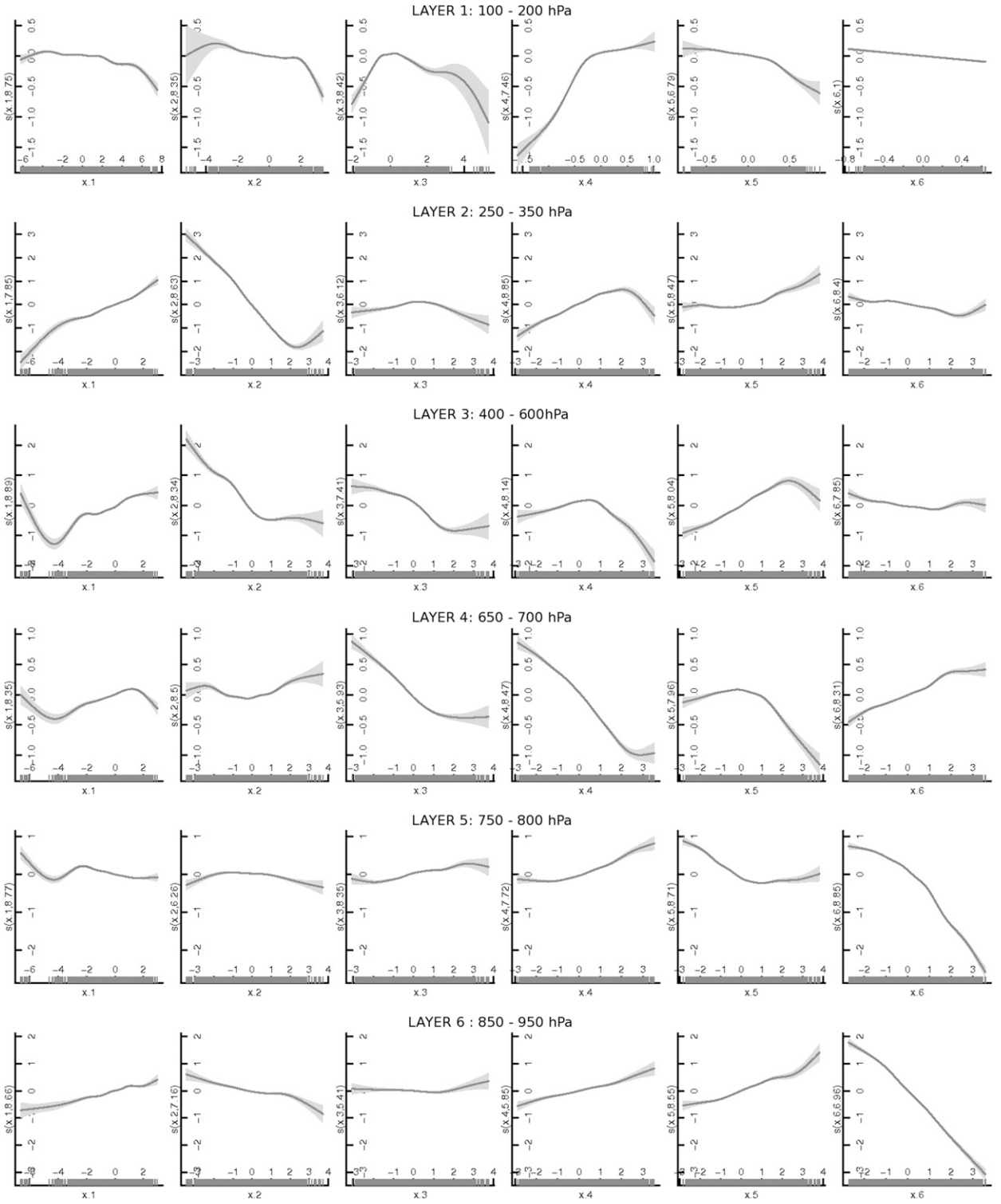

FIG. 4. Smoothing functions (the f_p^k, selected as penalized regression cubic splines s_p) fitted for the six atmospheric layers [layer 1 (top row); layer 6 (bottom row)], using the six BTs of SAPHIR as explanatory variables ($x_1, \ldots, x_6 = 183.31 \pm 0.2 \ldots 183.31 \pm 11$ GHz, normalized). The light gray shaded areas correspond to two standard errors above and below the estimated splines, and the gray ticks on the x axis give the predictor values from the training database. The numbers indicated in parentheses are the estimated degrees of freedom for each function.

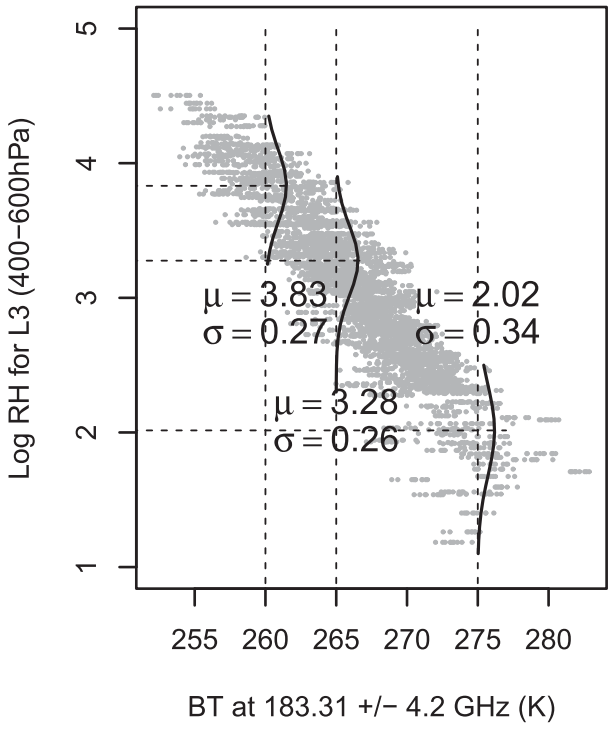

FIG. 5. Distribution of the average RH (%, with a log scale) of layer 3 (400–600-hPa layer) according to the BT of SAPHIR channel 4 (183.31 ± 4.2 GHz), taken from the training set. The conditional distributions, assuming a Gaussian law, of the RH given three different BTs (260, 265, and 275 K) are drawn as an example, and the corresponding μ and σ are indicated.

different uncertainties between the two situations, although with the same input vector.

b. *Estimation of the conditional uncertainties linked to the retrieval algorithm*

The additive framework allows for studying the accuracy of the relationship $RH^k = f_i^k(BT_i)$, and to do so for each i. Figure 5 is an illustration of such a relationship between the RH^3 (the 400–600-hPa layer, in log scale) and the BT_4 (183.31 ± 4.2 GHz), as observed in the training set. Obviously there is a scatter and the modeling of the distribution of RH^3 for particular values of BT_4 can be explored to have an estimate of the fitting uncertainty between BT_4 and RH^3. Therefore, if we assume that the conditional distributions of RH^3 given BT_4 follow Gaussian laws, then the estimation of the two parameters of the distributions—that is, the means μ and the standard deviations σ—is enough to characterize the retrieval uncertainty $RH^3 = f^3(BT_4)$. Examples of conditional distributions are provided for three BT_4 (260, 265, and 275 K), together with their μ and σ. One can thus see that the relationship $RH^3 = f^3(BT_4)$ cannot be characterized with only one distribution, since the values of σ depend on the BT_4. Such study can be propagated with p predictors (in the present case we have six BTs) thanks to the generalized additive model for location, scale and shape (GAMLSS) method (Rigby and Stasinopoulos 2005; Yan and Gebremichael 2009). It is an extension of the GAM framework that gives access to the distribution parameters of the regression: the mean (the *location*), the standard deviation (the *scale*), and the skewness and kurtosis (the two *shape* parameters). Because we work with Gaussian distributions, the two shape parameters are put aside in the following. As in GAMs, a GAMLSS-based regression assumes that the structure of each predictor is additive, so that each explanatory variable can include a wide variety of terms, parametric or not, such as penalized splines. The estimation of GAMLSS coefficients (such as the degree of smoothness of the splines) is based on penalized likelihood maximization (discussed at length in Rigby and Stasinopoulos 2005). Thus, instead of providing the best estimate of RH^k for k given **BT**, the GAMLSS approach gives the parameters of the conditional distribution of RH^k given **BT**, under the assumption that they have the same parametric form (a Gaussian law):

$$f(RH^k \mid \mathbf{BT}) = \frac{1}{\sigma\sqrt{2\pi}} \exp\left[-\frac{(RH^k - \mu_{\mathbf{BT}})^2}{2\sigma_{\mathbf{BT}}^2}\right], \quad (2)$$

where $\mu_{\mathbf{BT}}$ is the mean and $\sigma_{\mathbf{BT}}$ is the standard deviation of the distribution, which are both conditional on **BT**. In the following, for a given k $\mu_{\mathbf{BT}}$ will be referred to as the "estimated RH^k."

The method is called atmospheric relative humidity profiles including analysis of confidence intervals (ARPIA): for every set of BTs observed by SAPHIR, ARPIA computes the means and the standard deviations (also interpreted as the 1σ confidence interval) of the distributions of the possible estimates of the RH^k ($k = 1, \ldots, 6$).

Table 1 gives the statistical characteristics of the six GAMLSS over the ARSA subset of profiles not used for the training (a third of the initial database). This is to test the internal consistency of the training. The model validation is performed with the computation of the mean and the standard deviation of the error (observed minus estimated RH^k) for each k, and with the Pearson correlation coefficient (linear assumption). The continental scenes exhibit larger biases below 750 hPa (layers 5 and 6), nevertheless with quite high values of linear correlations (above 0.70). The best retrievals are obtained between 250 and 600 hPa, where the highest correlation coefficients (above 0.93) are associated with the lowest values of errors (means $< 1.8\%$) and standard deviations ($<5.2\%$). This is consistent with the findings of

Kumar et al. (2014) for the retrieval scheme layer-averaged relative humidity (LARH) detailed by Gohil et al. (2013) (the Indian scenario for SAPHIR) when compared to NWP model profiles.

c. *Evaluation using radiosonde profiles: Propagation of uncertainties*

We now consider the uncertainties of measurements using in situ probes in order to apply a model of propagation of error. Indeed, since for every atmospheric layer ARPIA provides a RH^k value together with its 1σ confidence of interval, the comparison to a reference (the RS measurement) should be an RH value associated with an uncertainty.

The quality of the thermodynamic profiles measured by the RS92 probes has been extensively studied, which yielded characterizing and correcting the biases (Vömel et al. 2007; Immler et al. 2010; Dirksen et al. 2014) and documenting the residual uncertainties. The work by Miloshevich et al. (2009) mentions two terms that affect the measured RH at a given point i: 1) a random term ε_1 induced by the variability of the sensor production, which is relative to the humidity conditions ($\varepsilon_1 = \pm 0.015 \times \mathrm{RH}$ for $\mathrm{RH} > 10\%$; $\varepsilon_1 = \pm 0.03 \times \mathrm{RH}$ for $\mathrm{RH} < 10\%$); and 2) a ground-check calibration uncertainty term ε_2 different between day ($\varepsilon_2 = \pm 0.05 \times \mathrm{RH} + 0.5$) and night ($\varepsilon_2 = \pm 0.04 \times \mathrm{RH} + 0.5$). As discussed in Clain et al. (2015) and following Immler et al. (2010), these individual uncertainties can be reasonably considered as random and independent, and thus sum up for a total measurement uncertainty at a given point as $\varepsilon_i = \sqrt{\varepsilon_1^2 + \varepsilon_2^2}$.

If RH^k is the mean relative humidity of a given k, estimated from $N = 50$ to 200 individual measurements of elementary rh_i ($i = 1, \ldots, N$), then the estimate of the variance (var) of the RH^k of the whole layer can be expressed as (BIPM 2008)

$$\widehat{\mathrm{var}(\mathrm{RH}^k)} = \mathrm{var}\left(\frac{1}{N}\sum_{i=1}^{N}\mathrm{rh}_i\right) = \frac{1}{N^2}\sum_{i=1}^{N}\mathrm{var}(\mathrm{rh}_i) + \frac{2}{N^2}\sum_{1\le i\le j\le N}\mathrm{covar}(\mathrm{rh}_i, \mathrm{rh}_j) \quad (3)$$

with covar as the covariance matrix between the rh_i. The analysis of the ε_i computed over the entire set of radiosoundings of the CDA experiment revealed very small variability, translating into $\mathrm{var}(\mathrm{rh}_i) = \varepsilon^2 \sim$ constant.

We can compute the lower and upper limits of the range of values that $\widehat{\mathrm{var}(\mathrm{RH}^k)}$ can take. If all of the rh_i are independent, then $\mathrm{covar}(\mathrm{rh}_i, \mathrm{rh}_j) = 0$ and the lower bound is given by

$$\widehat{\mathrm{var}(\mathrm{RH}^k)} = \frac{\varepsilon^2}{N}. \quad (4)$$

However, if all of the individual measurements are correlated to 1, then

$$R = \frac{\mathrm{covar}(\mathrm{rh}_i, \mathrm{rh}_j)}{\sqrt{\mathrm{var}(\mathrm{rh}_i)\,\mathrm{var}(\mathrm{rh}_j)}} = 1 \quad (5)$$

and it comes from Eq. (3) that the upper bound is

$$\widehat{\mathrm{var}(\mathrm{RH}^k)} = \varepsilon^2. \quad (6)$$

Thus, for each k the standard deviation associated with the averaged RH^k lies within

$$\frac{\varepsilon^2}{N} \le \widehat{\mathrm{var}(\mathrm{RH}^k)} \le \varepsilon^2. \quad (7)$$

In the following, we work with the upper-bound values, and the uncertainty will be noted as $\varepsilon^k_{\mathrm{RS}}$.

4. Application to *Megha-Tropiques* measurements

a. *Comparisons to upper-air soundings*

The comparison between the layer-averaged RH profiles given by ARPIA and the in situ estimates from the RS probe are performed following the method of Kelly (2007), and were recently applied by Roca et al. (2010) and Brogniez et al. (2015) to evaluate rainfall estimates and upper-tropospheric humidity estimates, respectively, from satellite observations. The method is described in the appendix.

The application of the method over the CDA dataset is illustrated in Fig. 6 with scatterplots of the observed layer-averaged RH from the RS probe versus the estimated RH from the ARPIA scheme [i.e., $\mu_{\mathbf{BT}}$ of Eq. (2)], including the representation of the uncertainties in both estimates [$\varepsilon_{\mathrm{RS}}$ and $\sigma_{\mathbf{BT}}$, respectively, in Eq. (2)]. The bias Δ and RMS of the regressions defined with the uncertainties are indicated ("err" subscript) together with the standard ("std" subscript) values for comparison purposes. There is a close correlation between the expectations, considering the distributions of the $\mathscr{J}_{\mathrm{RH}}$ of SAPHIR, and the results. Indeed ARPIA captures quite well the vertical variability of the RH contained in the RS, the smallest RMS, and the highest correlation coefficient R being reached at layers 2 (250–350 hPa) and 3 (400–600 hPa) with RMS = 7.58% RH and 6.52% RH and R = 0.89 and 0.93, respectively. This is induced, without any doubt, by the distribution of the $\mathscr{J}_{\mathrm{RH}}$: in these two layers the overlapping of the functions, and thus the information content of the BTs, is at its maximum, whereas for layers 4 (650–700 hPa) and 5 (750–800 hPa) the scatters are larger (RMS = 13% RH and

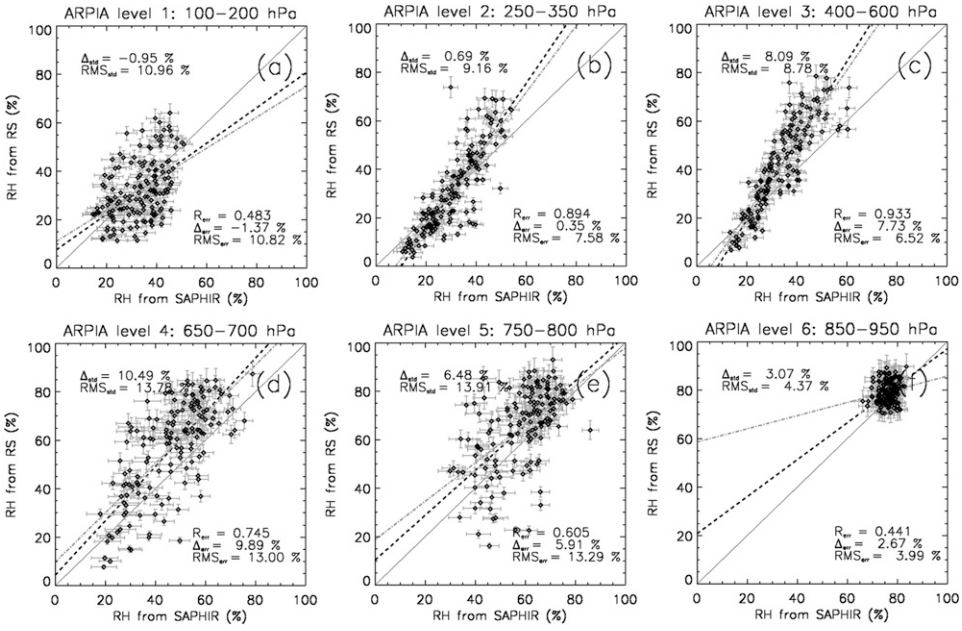

FIG. 6. Scatterplots of the RH (%) derived from SAPHIR BTs vs the RH from the RS profiles of the CDA soundings, for layers 1–6. Error bars related to the measured RH profile (vertical) and to the ARPIA retrieval (horizontal) are in gray. The gray dashed–dotted line is the standard regression line, and the black dashed line is the regression line accounting for errors. The mean bias (Δ) and RMS of the regression defined without (std subscript) and with (err subscript) the uncertainties are indicated, as well as *the coefficient of correlation R* and the $y = x$ line (gray).

13.29% RH, respectively). The ARPIA scheme is also able to reproduce the moist bottom layer 6 (850–950 hPa) of the RS, with the RMS being quite small (3.99% RH). The distance from the $y = x$ line is induced by the statistical constraints on the retrieval methodology.

A general summary that includes the statistical scores obtained over the Ouagadougou RS is provided in Table 2. Globally, the method produces a slightly biased midtroposphere (9.19% RH in the 400–600-hPa layer and 9.79% RH in the 650–700-hPa layer) with RMS below 12.12% RH, comparable to other techniques reaching an RMS of ~10% RH in the midtroposphere (Aires et al. 2013; Gohil et al. 2013). One can refer to Sivira et al. (2015) for a discussion on the improvements brought by the microwave imager Microwave Analysis and Detection of Rain and Atmospheric Systems (MADRAS), which is also part of the *Megha-Tropiques* payload and was declared nonoperational after almost 15 months of operations (a serious mechanical anomaly affecting the scan mechanism). The situations sampled during CDA are better reproduced by ARPIA than over Ouagadougou, which is most probably due to the small occurrence of Ouagadougoulike profiles within the training dataset sampled in ARSA. This assumption is reinforced by analysis of the mean RH profiles encompassed within the oceanic and continental training sets from ARSA and represented in Fig. 7, together with the RH profiles sampled during CDA and over Ouagadougou. While the oceanic set clearly includes the observations performed during CDA, the profiles measured over Ouagadougou are very marginal with respect to the continental set. This illustrates the need for a proper sampling of

TABLE 2. Biases (% RH), RMSE (% RH), and *R* estimated from the comparison between the RS and ARPIA over the six atmospheric layers, taking into account the uncertainties in both estimates (the statistics with the err subscript in Fig. 6). The two sets of RS are considered in a common block and separated.

Layer	Bias (% RH)	RMS (% RH)	*R*
100–200 hPa (L1)	−1.00	9.96	0.55
CDA/Ouagadougou	−1.37/−0.08	10.82/7.02	0.48/0.71
250–350 hPa (L2)	1.93	8.36	0.89
CDA/Ouagadougou	0.35/6.61	7.58/9.37	0.89/0.88
400–600 hPa (L3)	9.19	7.09	0.93
CDA/Ouagadougou	7.73/13.47	6.52/9.92	0.93/0.84
650–700 hPa (L4)	9.79	12.12	0.76
CDA/Ouagadougou	9.89/9.70	13.00/10.08	0.75/0.75
750–800 hPa (L5)	5.47	13.32	0.61
CDA/Ouagadougou	5.91/4.38	13.29/13.78	0.61/0.59
850–950 hPa (L6)	−0.56	1.58	0.98
CDA/Ouagadougou	2.67/−6.52	3.99/2.93	0.44/0.97

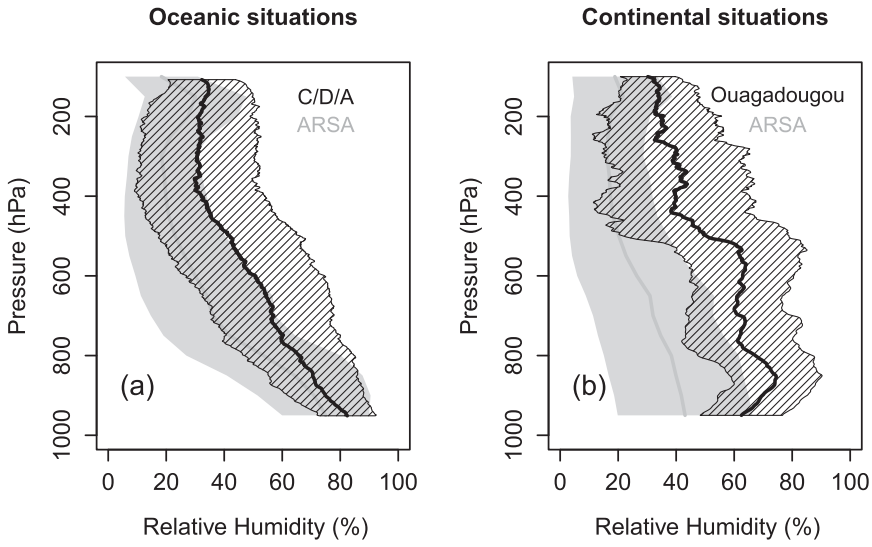

FIG. 7. Averaged RH profiles and their standard deviations contained in the ARSA training set over (a) the oceans and (b) the continents, together with the RS profiles of the two validation sets (CDA for the oceanic cases and Ouagadougou for the continental cases).

all atmospheric conditions when designing retrieval schemes based on statistical training. This is a difficult task when considering the current network of high-quality RS over the globe (Ciesielski et al. 2012), and actions toward a comprehensive database of RH profiles with traceability and the best possible characterization of uncertainties are currently done through comprehensive networks such as the Global Climate Observing System (GCOS) Reference Upper-Air Network (GRUAN; Dirksen et al. 2014; Bodeker et al. 2015).

b. *Comparisons to ECMWF profiles*

Six-hourly thermodynamic profiles produced on a 1° × 1° regular grid by the Integrated Forecast System (IFS) of the European Centre for Medium-Range Weather Forecasts (ECMWF) analyses (Uppala et al. 2005) have been interpolated onto every SAPHIR observation using the inverse distance weighting projection method and the 10 nearest neighbors. Then, four small regions (Fig. 8, upper panel) have been selected over the tropical belt, with only one surface type: central Africa (5°S–5°N, 20°–40°E), Indian Ocean (5°S–5°N, 60°–80°E), Pacific Ocean (0°–10°N, 170°–150°W), and Atlantic Ocean (15°–25°N, 40°–20°W). For each region, 100% of clear pixels and 100% of cloudy pixels (with no deep convective clouds nor ice layer), detected using the cloud analysis from the geostationnary observations, have been accumulated over the orbits associated with CDA-collocated RS, to reach 2048 valid profiles of ARPIA and ECMWF. The method of Kelly (2007) is again applied to compute the RMS between ARPIA and ECMWF for each atmospheric layer, assuming that the ECMWF RH profiles have no uncertainty. Figure 8 shows the profiles of RMS for the clear pixels and cloudy pixels, and for the four small regions. Under clear-sky conditions (assuming that all of the clouds are detected by the SAF NWC scheme, which is not the case; see the discussion in Sèze et al. 2015), the RMS is below 15% RH in general, with ECMWF and ARPIA profiles being in very good agreement (RMS < 5% RH) in the 400–600-hPa layer. Under overcast conditions the agreement is less obvious, with an overall RMS between 5% RH and 25% RH. Such distinction is also done by Bernardo et al. (2013), who found dispersions below 22% RH for cloudy-sky cases (maxima of RMS above 400 hPa) and an RH profile retrieval technique developed for the Humidity Sounder for Brazil (HSB) and the Advanced Microwave Scanning Radiometer for Earth Observing System (AMSR-E) instruments of the *Aqua* platform.

The four regions have a general consistency, but some discrepancies appear that require further investigation. For instance, for the clear-sky condition quite small RMS (<5% RH) are observed for the lowest layer over the central Africa and Indian Ocean regions, while it reaches values between 10% and 15% RH for the Pacific and Atlantic Ocean regions. This could be induced, for instance, by undetected low-level clouds by the SAF NWC algorithm, and the use of coincident CALIOP (and the onboard

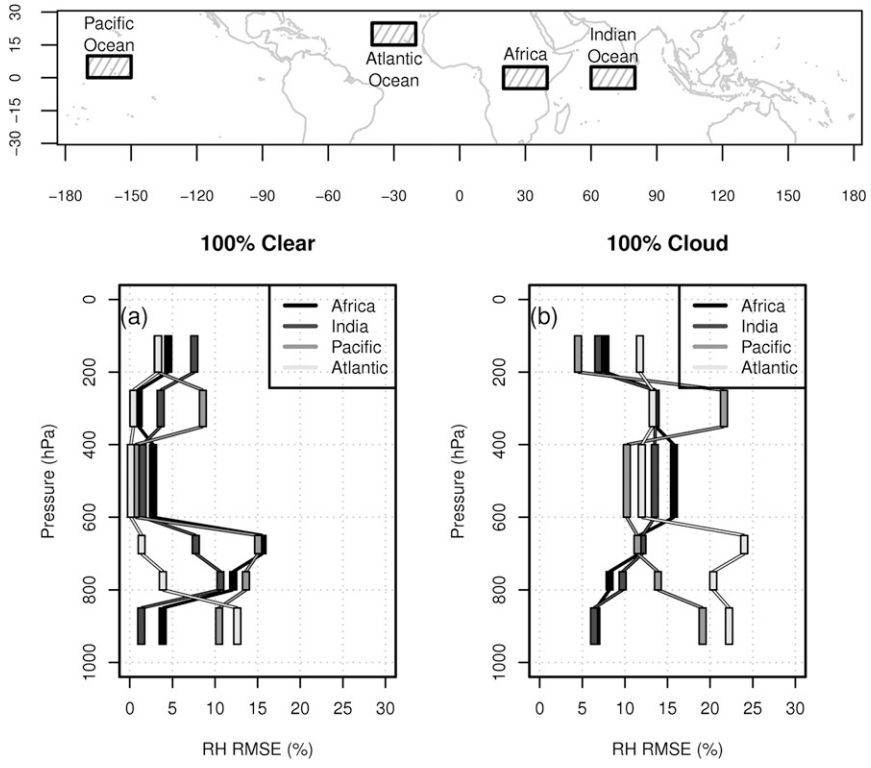

FIG. 8. Profiles of root-mean-square-errors (RMSE) defined from the comparison between collocated ECMWF RH profiles and ARPIA RH profiles. (top) The comparisons are performed over the four areas defined, for (a) clear-sky pixels and (b) overcast pixels.

CALIPSO) measurement would be a way to answer such an issue. A similar discrepancy is also visible in the cloudy situations for the same regions: ECMWF and ARPIA agree with an RMS around 6% RH in the central Africa and Indian Ocean regions, while the RMS is around 20% RH for the Pacific and Atlantic Ocean regions. This time, undetected low-level clouds cannot explain the difference and it most probably arises from the parameterization of shallow convective mixing in the ECMWF model (e.g., Webb et al. 2001; Hannay et al. 2009). These are interesting results since SAPHIR observations are not assimilated in the ECMWF IFS, thus calling for a dedicated study.

c. *An insight of the free-tropospheric humidity: In the vicinity of Tropical Cyclone Pam*

Tropical Cyclone Pam is a category 5 cyclone that appeared on 6 March 2015 and dissipated on 22 March 2015 in the western Pacific. It was observed by *Megha-Tropiques*, and it is used here as an application example for SAPHIR-derived RH profiles. Figure 9 shows the 10.8-μm observed BT by MTSAT at 0030 UTC 13 March 2015. On this date, the cyclone is located near the Vanuatu islands and the MTSAT observations reveal clearly the spatial extension of the phenomenon. The six-layer RH estimated from ARPIA and the corresponding σ are given in Fig. 10, as well as the closest RH field (0000 UTC, computed with respect to liquid water only) of the ECMWF interim reanalysis (ERA-Interim) model (Simmons et al. 2007). The cyclone is located near 170°E, indicated by a cross in the map presenting the RH of layer 4. SAPHIR is not yet assimilated into the IFS, which gives an independent observational tool to evaluate the tropospheric humidity of the model. One can see the filamentary structures of the water vapor field, and a clear drying from the bottom layer (850–950 hPa) up to the top layer (100–200 hPa). The rolling of moist air around the cyclone is visible until 250 hPa, hydration by intense cyclones noticed by previous studies (Folkins et al. 2002; Ray and Rosenlof 2007). The patterns of the conditional uncertainties σ associated with the retrieval of RH show that the largest σ are almost systematically associated with the driest structures. At first sight, the ERA-Interim RH fields present similar patterns: a dry tongue expands above Australia from the 750–800-hPa layer up to the 100–200-hPa layer with RH below 20%, a west–east

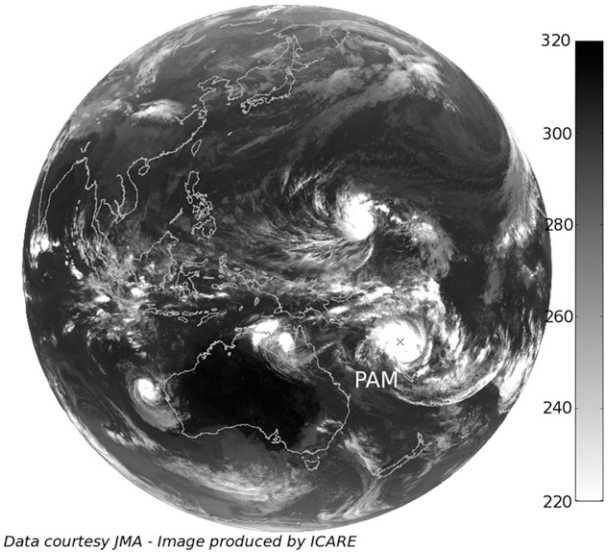

FIG. 9. The 10.8-μm BT measured by MTSAT at 0030 UTC 13 Mar 2015. Cyclone Pam is indicated by the cross.

(dry–moist) asymmetry surrounds the cyclone in the midtropospheric layers (700–250-hPa, layers 4–2), and a large moist area is located over Indonesia. The main discrepancies between ERA-Interim RH and SAPHIR RH are in the upper-tropospheric layer and in the lowest layer. Indeed, in the 350–100-hPa layer, the overall RH estimated from SAPHIR rarely exceeds 50%, while ERA-Interim produces RH fields that reach up to 80% in the 250–350-hPa layer and up to 60% in the 100–200-hPa layer.

An additional view is provided in Fig. 11 that presents the vertical distribution of the RH for the six layers, through the transect drawn in Fig. 10 (basically, the nadir line of the segment). To evaluate this small-scale variability, we have also represented the LARH estimation (the atmospheric layers are slightly different from ARPIA, and the retrieval is performed at the so-called L1A pixels, which are subject to a sampling overlap along the scan line, while ARPIA is applied to the so-called L1A2 pixels, where the overlap is removed), the corresponding field from ERA-Interim, and from the ECMWF operational analyses. The scan line associated with the position of Tropical Cyclone Pam is indicated. Artificial jumps are visible in the LARH retrieval and not in the ARPIA retrieval, which are not documented but may come from the L1A/L1A2 treatment. Several areas of vertical mixing are visible from the ARPIA retrieval: near 80°E above Sri Lanka, near 150°E above north of Australia, and near 175°E on the east side of the cyclone. These areas of mixing are also depicted by LARH, which confirms that such a pattern is contained in the SAPHIR observations. We also notice large structures of vertical drying, which are common within ECMWF (both ERA-Interim and the analyses) and within SAPHIR: at 130°E (Australia) and 160°E (western side of the cyclone). Discrepancies are also clear. For instance, estimates from SAPHIR give a quite dry upper layer (100–200 hPa) with an RH between 10% and 40% for ARPIA and LARH, while the ECMWF fields are significantly moister with an RH varying between 20% and 60%, even though the phasing is consistent. The lowest layer (850–950 hPa) is also very different between the two SAPHIR retrievals and the two ECMWF fields, the latter being slightly moister than the former with stronger variability: the strong drying near 150°E is produced through the whole troposphere, while estimates using the ARPIA scheme on SAPHIR do not produce such drying in this bottom layer. The origin of these differences needs to be further analyzed and understood.

5. Conclusions

Observations in the 183.31-GHz line are commonly used to perform RH profiling (Wilheit and Al Khalaf 1994; English 1999), and the novelty of the technique presented here lies in the conditional estimation of the parameters of the distribution, assuming a Gaussian law. The philosophy follows the work performed by Brogniez et al. (2013) and Sivira et al. (2015) with the training of generalized additive models to estimate six-layer-averaged RH profiles from the observations of the SAPHIR microwave radiometer. The six atmospheric layers are 100–200, 250–350, 400–600, 650–700, 750–800, and 850–950 hPa. The retrieval scheme atmospheric relative humidity profiles including analysis of confidence intervals (ARPIA) is used for the conditional mean and standard deviation of the distribution of the RH for each atmospheric layer. These datasets have been available to the international scientific community by the French ground segment of the *Megha-Tropiques* mission since July 2015 [Cloud–Aerosol–Water–Radiation Interactions (ICARE); http://www.icare.univ-lille1.fr/mt].

Two sets of tropical radiosoundings, an oceanic set and a continental set, already exploited within *Megha-Tropiques* for validation purposes (Clain et al. 2015; Brogniez et al. 2015; Sivira et al. 2015) are used to qualify the retrieval scheme. Overall, the biases range between −0.56% and 9.79%, the root-mean-square is below 13.32%, and the correlations coefficients are greater than 0.55 with a peak at 0.98. These performances are similar to other retrieval schemes developed for the operational radiometers Microwave Humidity Sounder (MHS)/AMSU-B (e.g., Aires

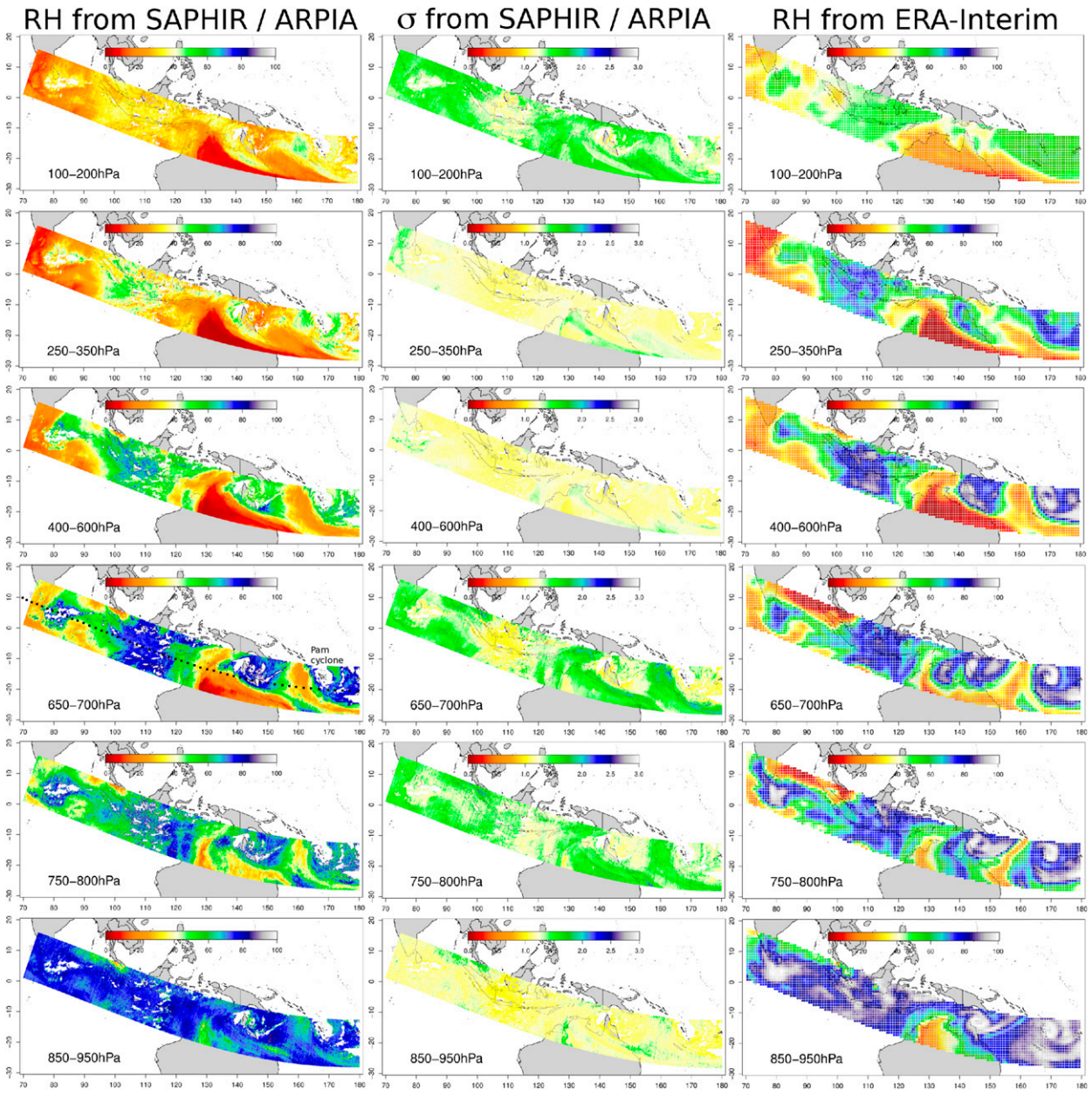

FIG. 10. Cyclone Pam as seen by SAPHIR, through the orbit of 0029 UTC 13 Mar 2015. The tropical cyclone is located at 15°S, 170°E. (left) RH, (middle) σ estimated by ARPIA, and (right) the ERA-Interim RH fields for the time step of 0000 UTC (0.75° grid). Each row corresponds to one atmospheric layer, as defined in Table 2.

et al. 2013), and a 1D variational technique should definitely improve the estimation of RH. The comparison of ARPIA layer-averaged RH and ECMWF RH fields (recall that ECMWF does not assimilate SAPHIR yet, although this is a current effort), taken from ERA-Interim and from the analyses, shows a nice consistency for the midtropospheric layers, despite significant discrepancies that are visible on the edge of the free troposphere.

The ARPIA scheme has nevertheless some issues that require dedicated studies:

- First, we used clear-sky RS to train the algorithm because the signature of clouds in the 183.31-GHz line is difficult to separate from the pure water vapor absorption, until the significant depression that occurs from the scattering by precipitating particles of deep convective clouds and upper-tropospheric icy layers

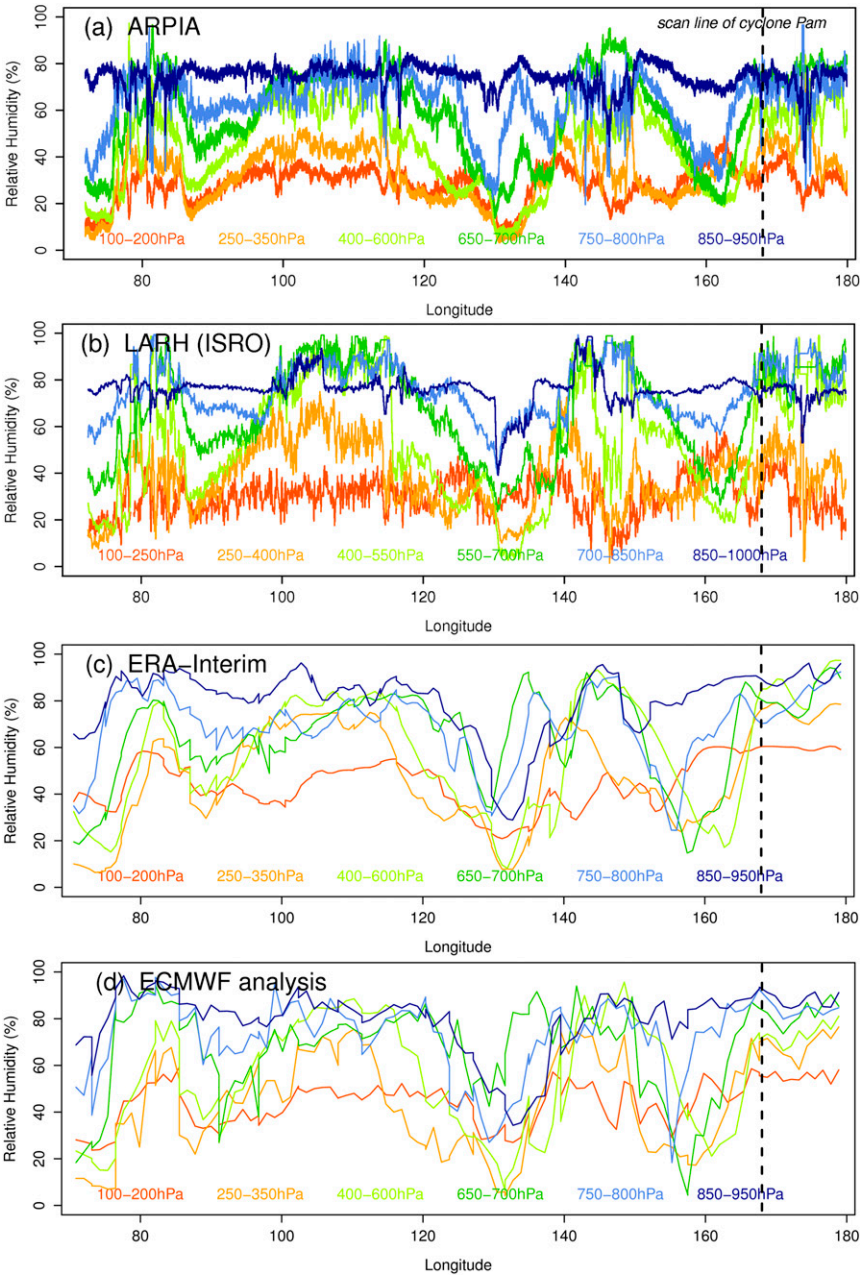

FIG. 11. Transect of RH estimated by (a) ARPIA and (b) the LARH retrieval from SAPHIR observations and provided by (c) ERA-Interim and (d) the operational ECMWF analyses. The transect goes through the middle of the swath (nadir view) along the orbit of 0029 UTC 13 Mar 2015, as drawn in Fig. 10, and the scan line containing Tropical Cyclone Pam is indicated. The thickness of ARPIA represents RH $\pm \sigma$. Note that the layers of LARH are slightly different.

(Rosenkranz et al. 1982; Greenwald and Christopher 2002). As mentioned in the core of the paper, the detection method exists for these clouds, but consideration of the remaining scenes requires a realistic training database that combines in situ measurements of the thermodynamic state and the cloudy air masses (liquid and ice water contents). Such profiles could be extracted from the ECMWF model, but their evaluation by Delanoë et al. (2011) using the ice water path (IWP) derived from joint observations by *CloudSat* and *CALIPSO* has revealed an overestimation of the thin and icy clouds associated with a too low global

IWP. Another way to address this issue would be to combine RS profiles and the cloud liquid and ice water contents derived from *CloudSat* and *CALIPSO* observations. Although a large number of representative situations are required in statistical training, the more than 10 years of observations by these instruments should be explored along that path and would offer a set of consistent and realistic thermodynamic profiles.

- Second, the geographic distribution of the RS used for the training should also be addressed: large regions of the tropics are not sampled [see, for instance, the Integrated Global Radiosonde Archive (IGRA) of NOAA that collects the operational RS transmitted of the Global Telecommunication System (GTS; Durre et al. 2006)], and although the ARSA database also gathers the RS launched during campaigns, the issue associated with the sampling of all the situations cannot be ruled out.
- Finally, the estimation of the algorithmic uncertainty is done under the strict symmetry imposed by a Gaussian distribution in the **BT**-to-RH transfer function. Therefore, one perspective is to fully explore the capacities of the GAMLSS framework in order to look at the shape parameters of the conditional distributions of RH—namely, the skewness and kurtosis—and test the modelization using a Gamma law assumption. Such a law would be indeed more appropriate and should improve the retrieval and provides uncertainty estimates closer to the true state.

Acknowledgments. The authors thanks the ClimServ team for its help with the handling of the data, as well as Michel Dejus and his team at CNES in the successive reprocessing of the *Megha-Tropiques* data since the launch. Overall, CNES is acknowledged for its financial support of the scientific activities of the *Megha-Tropiques* mission.

Nicolas Henriot from ICARE is thanked as well as the full staff of ICARE for the support of the *Megha-Tropiques* products and the processing of ARPIA. The French Institut de Recherche pour le Développement (IRD) and Agence pour la Sécurité de la Navigation Aérienne en Afrique et à Madagascar (ASECNA) are also thanked for their help in the organization of the Ouagadougou campaign. The help of R. Johnson, P. Ciesielski (CSU), and J. Wang (University at Albany, State University of New York) with the CINDY2011–DYNAMO–AMIE radiosounding dataset was greatly appreciated. The MOSDAC is also kindly acknowledged for the dissemination of the LARH product.

APPENDIX

Regression Taking Account of Uncertainties

The method is fully detailed in Kelly (2007). Here is a brief description: for two variables x_i and y_i with known uncertainties ε_x^i and ε_y^i that are both characterized by a Gaussian distribution, with respective variances S_x^i and S_y^i, and then the relationship between the vectors **x** and **y** can be expressed as

$$y_i + \varepsilon_y^i = \alpha + \beta(x_i + \varepsilon_x^i) + \varepsilon_i. \tag{A1}$$

The intrinsic scatter at i of the relationship is enclosed into the random variable ε^i, and the pair (α, β) represent the coefficients of the regression. As underlined by Kelly (2007), uncertainties in the measurements of variables have a spurious increasing/decreasing effect on the correlation between two variables, and its magnitude will depend on the value of the uncertainties with respect to the observed variances in **x** and **y**. A Bayesian method is used to solve the linear regression between vectors **x** and **y** accounting for the uncertainties using the computation of the maximum likelihood function of the data.

Using this method, the elements of comparisons between **x** and **y** are given with respect to the regression lines (with slope α and intercept β):

- the bias of the regression $\Delta = \beta + \bar{\mathbf{x}}(\alpha - 1)$, with $\bar{\mathbf{x}}$ referring to the mean value of **x**,
- the root-mean-square of the regression RMS $= \sqrt{1 - R^2} \times \sqrt{S_\mathbf{y}}$, with $S_\mathbf{y}$ referring to the variance of **y** and R is the correlation coefficient.

REFERENCES

Aires, F., F. Bernardo, and C. Prigent, 2013: Atmospheric water-vapour profiling from passive microwave sounders over ocean and land. Part I: Methodology for the Megha-Tropiques mission. *Quart. J. Roy. Meteor. Soc.*, **139**, 852–864, doi:10.1002/qj.1888.

Allan, R., 2012: The role of water vapour in Earth's energy flows. *Surv. Geophys.*, **33**, 557–564, doi:10.1007/s10712-011-9157-8.

——, K. Shine, A. Slingo, and J. Pamment, 1999: The dependence of clear-sky outgoing longwave radiation on surface temperature and relative humidity. *Quart. J. Roy. Meteor. Soc.*, **125**, 2103–2126, doi:10.1002/qj.49712555809.

Andersson, E., and Coauthors, 2005: Assimilation and modeling of the atmospheric hydrological cycle in the ECMWF forecasting system. *Bull. Amer. Meteor. Soc.*, **86**, 387–402, doi:10.1175/BAMS-86-3-387.

——, and Coauthors, 2007: Analysis and forecast impact of the main humidity observing systems. *Quart. J. Roy. Meteor. Soc.*, **133**, 1473–1485, doi:10.1002/qj.112.

Bernardo, F., F. Aires, and C. Prigent, 2013: Atmospheric water-vapour profiling from passive microwave sounders

over ocean and land. Part II: Validation using existing instruments. *Quart. J. Roy. Meteor. Soc.*, **139**, 865–878, doi:10.1002/qj.1946.

BIPM, 2008: Evaluation of measurement data—Guide to the expression of uncertainty on measurement. Working Group 1, Joint Committee for Guides in Metrology Doc. JCGM 100: 2008, 120 pp.

Blackwell, W., and F. Chen, 2006: Neural network retrieval of atmospheric temperature and moisture profiles from AIRS/AMSU data in the presence of clouds. *Algorithms and Technologies for Multispectral, Hyperspectral, and Ultraspectral Imagery XII*, S. S. Shen and P. E. Lewis, Eds., International Society for Optical Engineering (SPIE Proceedings, Vol. 6233), 62331E, doi:10.1117/12.664712.

Blankenship, C. B., A. Al-Khalaf, and T. T. Wilheit, 2000: Retrieval of water vapor profiles using SSM/T-2 and SSM/I data. *J. Atmos. Sci.*, **57**, 939–955, doi:10.1175/1520-0469(2000)057<0939:ROWVPU>2.0.CO;2.

Bodeker, G., and Coauthors, 2015: Reference upper-air observations for climate: From concept to reality. *Bull. Amer. Meteor. Soc.*, **97**, 123–135, doi:10.1175/BAMS-D-14-00072.1.

Bretherton, C., M. Peters, and L. Back, 2004: Relationships between water vapor path and precipitation over the tropical oceans. *J. Climate*, **17**, 1517–1528, doi:10.1175/1520-0442(2004)017<1517:RBWVPA>2.0.CO;2.

Brogniez, H., R. Roca, and L. Picon, 2009: A study of the free tropospheric humidity interannual variability using Meteosat data and an advection–condensation transport model. *J. Climate*, **22**, 6773–6787, doi:10.1175/2009JCLI2963.1.

——, P.-E. Kirstetter, and L. Eymard, 2013: Expected improvements in the atmospheric humidity profile retrieval using the Megha-Tropiques microwave payload. *Quart. J. Roy. Meteor. Soc.*, **139**, 842–851, doi:10.1002/qj.1869.

——, G. Clain, and R. Roca, 2015: Validation of upper-tropospheric humidity from SAPHIR on board *Megha-Tropiques* using tropical soundings. *J. Appl. Meteor. Climatol.*, **54**, 896–908, doi:10.1175/JAMC-D-14-0096.1.

Buehler, S., M. Kuvatov, V. John, M. Milz, B. J. Soden, D. Jackson, and J. Notholt, 2008: An upper tropospheric humidity data set from operational satellite microwave data. *J. Geophys. Res.*, **113**, D14110, doi:10.1029/2007JD009314.

Burns, B., X. Wu, and G. Diak, 1997: Effects of precipitation and cloud ice on brightness temperatures in AMSU moisture channels. *IEEE Trans. Geosci. Remote Sens.*, **35**, 1429–1437, doi:10.1109/36.649797.

Cabrera-Mercader, C., and D. Staelin, 1995: Passive microwave relative humidity retrievals using feedforward neural networks. *IEEE Trans. Geosci. Remote Sens.*, **33**, 1324–1328, doi:10.1109/36.477189.

Chae, J., D. Wu, W. Read, and S. Sherwood, 2011: The role of tropical deep convective clouds on temperature, water vapor and dehydration in the tropical tropopause layer (TTL). *Atmos. Chem. Phys.*, **11**, 3811–3821, doi:10.5194/acp-11-3811-2011.

Ciesielski, P., P. Haertel, R. Johnson, J. Wang, and S. Loehrer, 2012: Developing high-quality field program sounding datasets. *Bull. Amer. Meteor. Soc.*, **93**, 325–336, doi:10.1175/BAMS-D-11-00091.1.

——, and Coauthors, 2014: Quality-controlled upper-air sounding dataset for DYNAMO/CINDY/AMIE: Development and corrections. *J. Atmos. Oceanic Technol.*, **31**, 741–764, doi:10.1175/JTECH-D-13-00165.1.

Clain, G., H. Brogniez, V. H. Payne, V. O. John, and L. Ming, 2015: An assessment of SAPHIR calibration using quality tropical soundings. *J. Atmos. Oceanic Technol.*, **32**, 61–78, doi:10.1175/JTECH-D-14-00054.1.

Cole, T., and P. Green, 1992: Smoothing reference centile curves: The LMS method and penalized likelihood. *Stat. Med.*, **11**, 1305–1319, doi:10.1002/sim.4780111005.

Deblonde, G., and S. J. English, 2000: Evaluation of the FASTEM-2 fast microwave oceanic surface emissivity model. *Proc. 11th Television Infrared Observation Satellite Operational Vertical Sounder (TOV) Study Conferences*, Budapest, Hungary, WMO, 67–78.

Delanoë, J., R. Hogan, R. Forbes, A. Bodas-Salcedo, and T. Stein, 2011: Evaluation of ice cloud representation in the ECMWF and UK Met Office models using CloudSat and SALIPSO data. *Quart. J. Roy. Meteor. Soc.*, **137**, 2064–2078, doi:10.1002/qj.882.

Dirksen, R., M. Sommer, F. Immler, D. Hurst, R. Kivi, and H. Vömel, 2014: Reference quality upper-air measurements: GRUAN data processing for the Vaisala RS92 radiosonde. *Atmos. Meas. Tech.*, **7**, 4463–4490, doi:10.5194/amt-7-4463-2014.

Durre, I., R. Vose, and D. Wuertz, 2006: Overview of the Integrated Global Radiosonde Archive. *J. Climate*, **19**, 53–68, doi:10.1175/JCLI3594.1.

English, S., 1999: Estimation of temperature and humidity profile information from microwave radiances over different surface types. *J. Appl. Meteor.*, **38**, 1526–1541, doi:10.1175/1520-0450(1999)038<1526:EOTAHP>2.0.CO;2.

Folkins, I., K. Kelly, and E. Weinstock, 2002: A simple explanation for the increase in relative humidity between 11 and 14 km in the tropics. *J. Geophys. Res.*, **107**, 4736, doi:10.1029/2002JD002185.

Galewsky, J., A. Sobel, and I. Held, 2005: Diagnosis of subtropical humidity dynamics using tracers of last saturation. *J. Atmos. Sci.*, **62**, 3353–3367, doi:10.1175/JAS3533.1.

Gohil, B., R. Gairola, A. Mathur, A. Varma, C. Mahesh, R. Gangwar, and P. Pal, 2013: Algorithms for retrieving geophysical parameters from the MADRAS and SAPHIR sensors of the Megha-Tropiques satellites: Indian scenario. *Quart. J. Roy. Meteor. Soc.*, **139**, 954–963, doi:10.1002/qj.2041.

Greenwald, T., and S. Christopher, 2002: Effect of cold clouds on satellite measurements near 183 GHz. *J. Geophys. Res.*, **107**, 4170, doi:10.1029/2000JD000258.

Hakkarinen, I., and R. Adler, 1988: Observations of precipitating convective systems at 92 and 183 GHz: Aircraft results. *Meteor. Atmos. Phys.*, **38**, 164–182, doi:10.1007/BF01029780.

Hannay, C., D. Williamson, J. Hack, J. Kiehl, J. Olson, S. Klein, C. Bretherton, and M. Kohler, 2009: Evaluation of forecasted southeast Pacific stratocumulus in the NCAR, GFDL, and ECMWF models. *J. Climate*, **22**, 2871–2889, doi:10.1175/2008JCLI2479.1.

Hastie, T., and R. Tibshirani, 1987: Generalized additive models: Some applications. *J. Amer. Stat. Assoc.*, **82**, 371–386, doi:10.1080/01621459.1987.10478440.

——, and ——, 1990: *Generalized Additive Models*. Monographs on Statistics and Applied Probability, Vol. 43, Chapman & Hall/CRC, 352 pp.

Held, I., and B. Soden, 2000: Water vapour feedback and global warming. *Annu. Rev. Energy Environ.*, **25**, 441–475, doi:10.1146/annurev.energy.25.1.441.

——, and ——, 2006: Robust responses of the hydrological cycle to global warming. *J. Climate*, **19**, 5686–5699, doi:10.1175/JCLI3990.1.

Hong, G., G. Heygster, J. Miao, and K. Kunzi, 2005: Detection of tropical deep convective clouds from AMSU-B water vapor channels measurements. *J. Geophys. Res.*, **110**, D05205, doi:10.1029/2004JD004949.

——, G. Hegster, J. Notholt, and S. Buehler, 2008: Interannual to diurnal variations in tropical and subtropical deep convective clouds and convective overshooting from seven years of AMSU-B measurements. *J. Climate*, **21**, 4168–4189, doi:10.1175/2008JCLI1911.1.

Houshangpour, A., V. John, and S. Buehler, 2005: Retrieval of upper tropospheric water vapor and upper tropospheric humidity from AMSU radiances. *Atmos. Chem. Phys.*, **5**, 2019–2028, doi:10.5194/acp-5-2019-2005.

Immler, F. J., J. Dykema, T. Gardiner, D. N. Whiteman, P. W. Thorne, and H. Vömel, 2010: Reference quality upper-air measurements: Guidance for developing GRUAN data products. *Atmos. Meas. Tech.*, **3**, 1217–1231, doi:10.5194/amt-3-1217-2010.

Isaacs, R., and G. Deblonde, 1987: Millimeter wave moisture sounding: The effect of clouds. *Radio Sci.*, **22**, 367–377, doi:10.1029/RS022i003p00367.

John, V., and B. Soden, 2006: Does convectively-detrained cloud ice enhance water vapor feedback? *Geophys. Res. Lett.*, **33**, L20701, doi:10.1029/2006GL027260.

Karbou, F., F. Aires, C. Prigent, and L. Eymard, 2005: Potential of Advanced Microwave Sounding Unit-A (AMSU-A) and AMSU-B measurements for atmospheric temperature and humidity profiling over land. *J. Geophys. Res.*, **110**, D07109, doi:10.1029/2004JD005318.

Karouche, N., C. Goldstein, A. Rosak, C. Malassingne, and G. Raju, 2012: MEGHA-TROPIQUES satellite mission: In flight performances results. *IGARSS 2012: IEEE International Geoscience and Remote Sensing Symposium; Proceedings*, IEEE, 4684–4687, doi:10.1109/IGARSS.2012.6350420.

Kelly, B., 2007: Some aspects of measurement errors in linear regression of astronomical data. *Astrophys. J.*, **665**, 1489–1506, doi:10.1086/519947.

Kohonen, T., 1982: Self-organizing formation of topologically correct feature maps. *Biol. Cybern.*, **43**, 59–69, doi:10.1007/BF00337288.

Kumar, P., S. Deb, R. Ganwar, B. Simon, and P. K. Pal, 2014: Layer average relative humidity from SAPHIR on board Megha-Tropiques: Validation with numerical model analyses. *Int. J. Remote Sens.*, **35**, 4839–4851, doi:10.1080/01431161.2014.930204.

Liu, Q., and F. Weng, 2005: One-dimensional variational retrieval algorithm of temperature, water vapor and cloud water profiles from Advanced Microwave Sounding Unit (AMSU). *IEEE Trans. Geosci. Remote Sens.*, **43**, 1087–1095, doi:10.1109/TGRS.2004.843211.

Matricardi, M., F. Chevallier, G. Kelly, and J. Thépaut, 2004: An improved general fast radiative transfer model for the assimilation of radiance observations. *Quart. J. Roy. Meteor. Soc.*, **130**, 153–173, doi:10.1256/qj.02.181.

Miloshevich, L., H. Vömel, D. Whiteman, and T. Leblanc, 2009: Accuracy assessment and correction of Vaisala RS92 radiosonde water vapor measurements. *J. Geophys. Res.*, **114**, D11305, doi:10.1029/2008JD011565.

Nalli, N., and Coauthors, 2013: Validation of satellite sounder environmental data records: Application to the Cross-Track Infrared Microwave Sounder Suite. *J. Geophys. Res. Atmos.*, **118**, 13 628–13 643, doi:10.1002/2013JD020436.

Pierrehumbert, R., 2011: Infrared radiation and planetary temperature. *Phys. Today*, **64**, 33–38, doi:10.1063/1.3541943.

——, and R. Roca, 1998: Evidence for control of Atlantic subtropical humidity by large-scale advection. *Geophys. Res. Lett.*, **25**, 4537–4540, doi:10.1029/1998GL900203.

Prigent, C., F. Aires, and W. Rossow, 2006: Land surface microwave emissivities over the globe for a decade. *Bull. Amer. Meteor. Soc.*, **87**, 1573–1584, doi:10.1175/BAMS-87-11-1573.

Radnóti, G., P. Bauer, A. MacNally, C. Cardinati, S. Healy, and P. de Rosnay, 2010: ECMWF study on the impact of future developments of the space-based observing system on Numerical Weather Prediction. ECMWF Tech. Memo. 638, 115 pp.

Ray, E., and K. Rosenlof, 2007: Hydration of the upper troposphere by tropical cyclones. *J. Geophys. Res.*, **112**, D12311, doi:10.1029/2006JD008009.

Rigby, R. A., and D. M. Stasinopoulos, 1996: A semi-parametric additive model for variance heterogeneity. *Stat. Comput.*, **6**, 57–65, doi:10.1007/BF00161574.

——, and ——, 2005: Generalized additive models for location, scale and shape. *J. Roy. Stat. Soc.*, **54A**, 507–554, doi:10.1111/j.1467-9876.2005.00510.x.

Roca, R., J.-P. Lafore, C. Piriou, and J.-L. Redelsperger, 2005: Extratropical dry-air intrusions into the West African monsoon midtroposphere: An important factor for the convective activity over the Sahel. *J. Atmos. Sci.*, **62**, 390–407, doi:10.1175/JAS-3366.1.

——, and Coauthors, 2010: On the water and energy cycles in the Tropics. *C. R. Geosci.*, **342**, 390–402, doi:10.1016/j.crte.2010.01.003.

——, and Coauthors, 2015: The Megha-Tropiques mission: A review after three years in orbit. *Front. Earth Sci.*, **3**, doi:10.3389/feart.2015.00017.

Rosenkranz, P., M. Komichak, and D. Staelin, 1982: A method for estimation of atmospheric water vapor profiles by microwave radiometry. *J. Appl. Meteor.*, **21**, 1364–1370, doi:10.1175/1520-0450(1982)021<1364:AMFEOA>2.0.CO;2.

Schaerer, G., and T. T. Wilheit, 1979: A passive microwave technique for profiling of atmospheric water vapor. *Radio Sci.*, **14**, 371–375, doi:10.1029/RS014i003p00371.

Sèze, G., J. Pelon, M. Derrien, H. L. Gléau, and B. Six, 2015: Evaluation against CALIPSO lidar observations of the multi-geostationary cloud cover and type dataset assembled in the framework of the Megha-Tropiques mission. *Quart. J. Roy. Meteor. Soc.*, **141**, 774–797, doi:10.1002/qj.2392.

Sherwood, S., R. Roca, T. Weckwerth, and N. Andronova, 2010: Tropospheric water vapor, convection and climate. *Rev. Geophys.*, **48**, RG2001, doi:10.1029/2009RG000301.

Simmons, A., S. Uppala, D. Dee, and S. Kobayashi, 2007: ERA-Interim: New ECMWF reanalysis products from 1989 onwards. *ECMWF Newsletter*, No. 110, ECMWF, Reading, United Kingdom, 25–35.

Sivira, R., H. Brogniez, C. Mallet, and Y. Oussar, 2015: A layer-averaged relative humidity profile retrieval for microwave observations: Design and results for the Megha-Tropiques payload. *Atmos. Meas. Tech.*, **8**, 1055–1071, doi:10.5194/amt-8-1055-2015.

Spencer, R., and W. Braswell, 1997: How dry is the tropical free troposphere? Implications for a global warming theory. *Bull. Amer. Meteor. Soc.*, **78**, 1097–1106, doi:10.1175/1520-0477(1997)078<1097:HDITTF>2.0.CO;2.

Stevens, B., and S. Bony, 2013: Water in the atmosphere. *Phys. Today*, **66**, 29–34, doi:10.1063/PT.3.2009.

Uppala, S., and Coauthors, 2005: The ERA-40 Re-Analysis. *Quart. J. Roy. Meteor. Soc.*, **131**, 2961–3012, doi:10.1256/qj.04.176.

Vömel, H., and Coauthors, 2007: Radiation dry bias of the Vaisala RS92 humidity sensor. *J. Atmos. Oceanic Technol.*, **24**, 953–963, doi:10.1175/JTECH2019.1.

Webb, M., C. Senior, C., S. Bony, and J.-J. Morcrette, 2001: Combining ERBE and ISCCP data to assess clouds in the Hadley Center, ECMWF and LMD atmospheric climate models. *Climate Dyn.*, **17**, 905–922, doi:10.1007/s003820100157.

Wilheit, T., 1990: An algorithm for retrieving water vapor profiles in clear and cloudy atmospheres from 183 GHz radiometric measurements: Simulation studies. *J. Appl. Meteor.*, **29**, 508–515, doi:10.1175/1520-0450(1990)029<0508:AAFRWV>2.0.CO;2.

——, and A. Al Khalaf, 1994: A simplified interpretation of the radiances from the SSM/T-2. *Meteor. Atmos. Phys.*, **54**, 203–212, doi:10.1007/BF01030060.

Wood, S., 2004: Stable and efficient multiple smoothing parameter estimation for generalized additive models. *J. Amer. Stat. Assoc.*, **99**, 673–686, doi:10.1198/016214504000000980.

——, 2006: *Generalized Additive Models: An Introduction with R*. Chapman & Hall/CRC Texts in Statistical Science, Vol. 66, Chapman & Hall/CRC, 410 pp.

Yan, J., and M. Gebremichael, 2009: Estimating actual rainfall from satellite rainfall products. *Atmos. Res.*, **92**, 481–488, doi:10.1016/j.atmosres.2009.02.004.

Zelinka, M., and D. Hartmann, 2009: Response of humidity and clouds to tropical deep convection. *J. Climate*, **22**, 2389–2404, doi:10.1175/2008JCLI2452.1.